Lithium Niobate ($LiNbO_3$) Waveguides for Electromagnetic Pulse (EMP) Sensing.

Andrew J. Waddie[1], Adrian Dzipalski[1], Iain Thurston[2], Michael Moutrie[2] and Mohammad R. Taghizadeh[1]
1 - Institute of Photonics and Quantum Sciences, School of Engineering and Physical Sciences, Heriot-Watt University, Riccarton, Edinburgh, EH14 4AS, United Kingdom.
2- Atomic Weapons Establishment, Aldermaston, Reading, Berkshire, RG7 4PR United Kingdom.

***Abstract*— In this paper we report on the fabrication and experimental verification of waveguide structures for electromagnetic pulse sensing (EMP). The waveguides were realized in z–cut Lithium Niobate ($LiNbO_3$) using e-beam and photolithographic technique followed by reactive ion etching processes. Channel structures with widths of 1 µm were etched and, after backfilling of the etched channels with amorphous silicon (a-Si), resulted in a single mode waveguide structure for operation at 1550nm. The fabricated devices have successfully measured both the peak field strength and the temporal pulse shape of a range of electromagnetic pulses.**

***Index Terms*— Coupled Mode Analysis, Electromagnetic Fields, Etching, Lithium Compounds, Lithography, Optical coupling, Optical device fabrication, Optical waveguides**.

I. INTRODUCTION

The detection of short duration electromagnetic pulses (EMP) with a double Gaussian temporal profile of up to a few hundred nanoseconds duration and a GHz center frequency, such as those produced in a typical lightning discharge event, is achieved conventionally using an electrical antenna based sensor[1]. These sensors which are capable of accurately measuring both the peak electric field strength of the EMP and the temporal profile of the pulse are macroscopic systems (with sizes comparable to several wavelengths of the central RF frequency) and can introduce significant perturbation of the EMP during measurement. The commercially available d-dot sensor measures the time derivate of the electric flux density on the surface of a conductor allowing the electric field profile to be calculated by integration of the measured signal. These sensors, which are capable of measuring the typical temporal electric field profiles under consideration, are subject to a number of limitations in performance and usage, most significantly in bandwidth, sensitivity and overall sensor size. The upper frequency bandwidth of a d-dot sensor is proportional to the reciprocal of the time constant of the complete electrical circuit of the sensor. In order to have a sensor capable of high frequency operation the low voltage capacitance of the sensor must be minimized, leading to reduced sensitivity at lower frequencies. By exploiting all-optical devices based around electro-optic materials and optical detection methods, a small-form factor, high bandwidth sensor can be designed offering the possibility of a significantly smaller sensor package with minimal potential for EMP perturbation.

Lithium Niobate ($LiNbO_3$) is a man-made, birefringent material possessing a large electro-optic tensor which offers a potential route to coupling an incident radio frequency (RF) EMP to an optical sensing system. Lithium Niobate can be used as a bulk electro-optic modulator [2], but integrated optical devices have the greatest potential for a high sensitivity, miniaturized sensor system primarily due to the increased nonlinear interaction arising from their small mode confinement volume. Integrated optical devices made from Lithium Niobate have already been employed in a wide range of application areas such as surface acoustic wave devices [3], electric field sensors [4] and photonic crystals [5].

A number of different methods for the fabrication of waveguide structures in Lithium Niobate have been described in the literature. Doping processes, using either titanium in-diffusion (TI) or annealled proton exchange (PX), have been used to create both planar and channel waveguides [6]. Titanium in-diffusion is the most widespread fabrication technique for Lithium Niobate waveguides and has been studied extensively since its introduction in the 1970's [7]. During in-diffusion, the electro-optic properties of the crystal are maintained and the final structures provide good optical confinement. Typical waveguide widths range from 5–10µm and overall waveguide depths from 30-100nm. Both the ordinary and extraordinary refractive indices are altered making in-diffused waveguides insensitive to the incident light polarization [8]. Proton exchange followed by annealing to recover those nonlinear coefficients compromised by the proton exchange process has been used to fabricate waveguide depths of up to 500nm. This fabrication method gives a much greater extraordinary refractive index change compared to Titanium in-diffusion [9], but is highly sensitive to the polarization of the incident light. Recently it has been demonstrated that waveguides may be fabricated by translating the transparent $LiNbO_3$ substrate through the focus of a femtosecond pulse train which induces changes in the refractive index of the material through laser

induced stress within the crystal matrix (FS) [10]. The waveguides produced by this fabrication method are limited by the optics of the laser exposure system and the accuracy of the translation hardware. Smart Cut (SC) or Crystal ion slicing [11] devices are formed from a thin (up to 1µm) $LiNbO_3$ film bonded to a SiO_2 layer of 50-100µm thickness which can then be attached to a carrier wafer to facilitate mechanical handling and processing. Waveguides with a width of about 800nm have been demonstrated with a high degree of optical confinement. Optical Grade dicing (OD) can also be used for the formation of waveguides [12] leading to the formation of ridge waveguides with widths and depths of 6µm and 10µm respectively. One of the major limitations of this technique is that the spacing between waveguides is limited by the width of the dicing saw blade used (~200µm). Table 1 shows a limited parameter comparison between these different waveguide fabrication methods and the method outlined in this paper (HW). For waveguide separation, a direct comparison between methods is not possible in each case due to a lack of suitable studies in the literature.

Waveguide Parameter	TD	PX	FS	SC	OD	HW
Depth (µm)	<0.1	<0.5	>8.0	<1.0	<10.0	<3.0
Width (µm)	>5.0	>1.0	>8.0	>0.8	>6.0	>1.0
Separation (µm)	X	X	>2.0	X	>200	>0.8
Polarisation	TM/TE	TM	TM	TM/TE	TM/TE	TM/TE
Δn (**L**ow/**M**ed/ **H**igh)	L	L	L	H	H	M

Table 1: Comparison of waveguide fabrication techniques.

In this paper we present a novel and inherently simple technique for the fabrication of leaky channel waveguides in Lithium Niobate through a combination of electron beam lithography, reactive ion etching, and backfilling deposition and lift off. A number of fabrication limitations, caused by the structure and chemistry of the Lithium Niobate, were identified and overcome during the development of the fabrication process.

II. DESIGN AND FABRICATION OF WAVEGUIDES

A. Modeling

The basic structure used to perform the EMP sensing is based around three waveguides placed in sufficiently close proximity to permit evanescent coupling [13] between the central input waveguide and the two side waveguides. This evanescent coupling is highly sensitive to the refractive index of the cladding material between the waveguides and, by using a material with a large electro-optic nonlinear refractive index, a device with an output that is a function of the applied electric field can be created.

The light that propagates through the waveguide has most of the power concentrated within the central core of the waveguide. In the cladding region the light intensity decays exponentially with distance from the core. Placing additional waveguides on either side of the central waveguide introduces a perturbation to the mode shape of the central waveguide and vice versa [16]. Instead of having two independent modes with the same effective index, one of which is localized in the central waveguide and the other in the adjacent waveguides, the modes and their effective indices couple and two super modes (symmetric[S] and antisymmetric [A]) are created with effective indices slightly larger (S) and lower (A) than the effective index of the unperturbed central waveguide mode. For the precise device geometry under consideration in this paper, the cladding is LiNbO3 (n=2.2111) and the core is a-Si (n=2.3343). The core cross section is square with a total size of 1µm x 1µm.The three waveguides are separated by a distance of 1 µm. Due to the a:Si deposition method used during fabrication, a thin bridge of a:Si is formed between the waveguides. The magnitude of the Poynting vectors along the direction of propagation of the antisymmetric and symmetric supermodes are shown in Fig. 1 and Fig. 2 respectively.

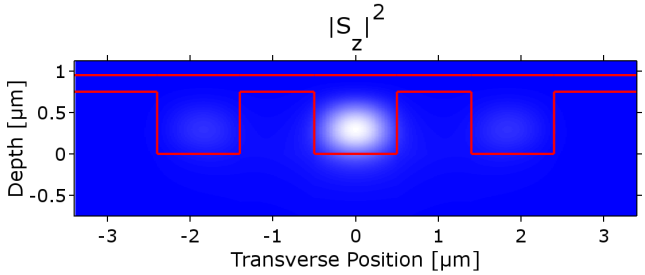

Fig. 1. Poynting vector magnitude of waveguide coupling structure showing the antisymmetric mode. The red lines delineate the areas of a-Si infill with the area below the lower line being the $LiNbO_3$ substrate and the area above the upper line being the SiO_2 carrier substrate (see Section II(B) for details of sensor assembly).

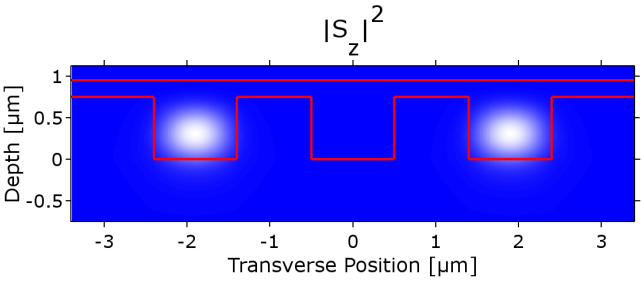

Fig. 2. Poynting vector magnitude of waveguide coupling structure showing the symmetric mode. The red lines show the waveguide infill as for Fig. 1.

The supermodes are both solutions to the wave equation and upon excitation will propagate unperturbed through the waveguide. When both symmetric and anti-symmetric modes are excited a beating effect is observed between the two modes and the power distribution between the individual waveguides changes as the incident light propagates through the structure. The length of the waveguide structure can be adjusted to ensure a specific level of coupling from the central waveguide to the adjacent waveguides. Due to the typical propagation length (300-850 µm) being much longer than the wavelength of the light propagated, the beam envelope method can be used to model the waveguide coupling as the computational mesh does not need to resolve on the wavelength scale but rather on the inter-super mode beating length scale [14].

The total electric field can be written as the sum of the electric fields of the two super modes;

$$E(z) = [E_1 + E_2 \exp(-i(\beta_A - \beta_S)y]\exp(-i\beta_S y) \quad (1)$$

Where E_1 and E_2 are the amplitudes of the two supermodes (and can be assumed to be identical), β_A and β_S are the propagation constants of the antisymmetric and symmetric supermodes respectively and y is the propagation distance along the waveguide.

The expression within the square parenthesis can be solved giving an expression for the coupling length (L) of

$$(\beta_A - \beta_S)L = 2\pi \quad (2)$$

Therefore;

$$L = \frac{2\pi}{(\beta_A - \beta_S)} \quad (3)$$

Fig. 3 shows the result of one of the mode propagation simulations. The red lines show the lateral extent of the waveguide cores (shown by the vertical red lines in Figs. 1 and 2). For this simulation the symmetric mode was found to have a refractive index of 2.2248 and the asymmetric mode has a refractive index of 2.2295.

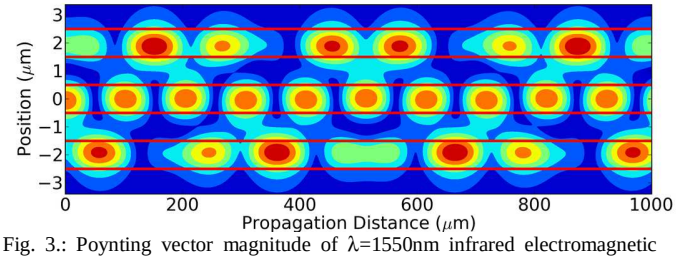

Fig. 3.: Poynting vector magnitude of λ=1550nm infrared electromagnetic radiation propagating through the waveguide coupling structure. The mode coupling between waveguides is shown in the depth = 0.33μm plane (cf. Fig. 1 and 2). The solid red lines delineate the cores of the waveguides.

The variation of the relative propagated light intensity between the central and side waveguides as a function of the applied external electric field can be determined from a series of simulations with the cladding refractive index calculated by;

$$n(E) = n_o + \frac{1}{2} r_{33} n_o^3 E_z \quad (4)$$

Where n0 is the ordinary refractive index of $LiNbO_3$ in the absence of external electric field, r_{33} is the z-field, z-directed component of the electro-optic tensor of $LiNbO_3$ (=30.9 pm/V) and E_z is the applied RF electric field.

For the field strengths required to be measured (50kV/m – 500 kV/m) Eq. 4 results in a change in refractive index on the order of 10^{-4} to 10^{-5}. The results of these simulations are shown in Fig. 4 for a total coupling length of 850μm – the measured parameter is the output intensity of both side waveguides relative to the output intensity of the same side waveguide under no applied electric field. It can be seen from this figure that the sensor shows a good response to the applied electric field (in the 5-10% range).

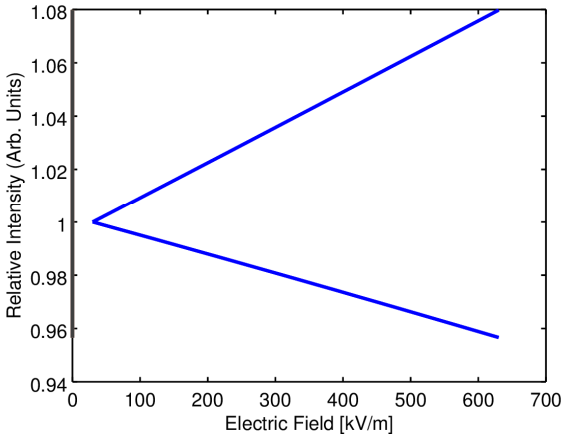

Fig. 4. Simulated relative intensity change from side channels of waveguide sensor as a function of applied electric field. The top line is the output from the left waveguide, the bottom line is the output from the right waveguide.

Table 2 below compares the operating parameters for a PRODYN free space d-dot electric field sensor with those for the waveguide sensor. The waveguide sensor is limited in terms of bandwidth and rise time by the detection electronics, in particular the photodiode used to convert the optical signal into an electrical signal.

Sensor	AD-20 (free space d-dot)	$LiNbO_3$ waveguide
Response	>10GHz	>0.63GHz
Rise Time	<.029ns	<1.57ns
Maximum Output	150V	1-5V
Mass	40 g	6.6g
Length	390.4mm	25mm
Breath	25.4mm	15mm
Height	10.9mm	8mm

Table 2: Comparison between commercially available d-dot sensor and fabricated $LiNbO_3$ waveguide sensor.

B. Fabrication

The fabrication of the waveguides is achieved by patterning the substrate through e-beam lithography using a Raith Pioneer 100 Scanning Electron Microscope with an-e beam lithography attachment. A layer of the conducting polymer PEDOT: PSS was used to prevent charging of the substrate during the patterning. This conducting polymer is easily removed after exposure as well as acting as an adhesion promotion layer to the negative tone e-beam resist (AZ-NLof 2070) used for the substrate patterning. The resist allows high precision pattern transfer via liftoff and high stability to the thermal softening which occurs during the deposition process. Fig. shows a schematic for the waveguide fabrication procedure and a phase-contrast micrograph of a completed waveguide structure is shown in Fig. 6.

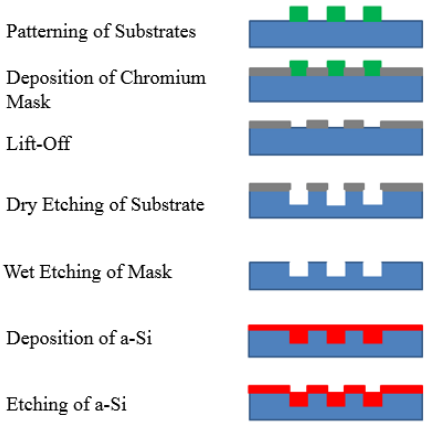

Fig. 5. Fabrication Steps involved in production of amorphous silicon waveguides in Lithium Niobate.

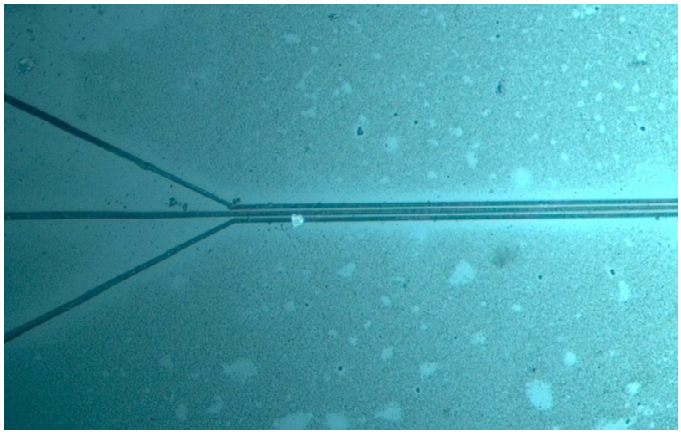

Fig. 6. Micrograph of part of the waveguide microstructure after processing under a phase contrast microscope at 50X magnification.

The etching of the Lithium Niobate is carried out using an Oxford Plasma 100 RIE-ICP machine. Lithium Niobate is etched using fluorine based chemistry and the etching recipe used is summarized as follows. Chamber conditions: 50mTorr striking pressure, 10mTorr chamber pressure. Plasma conditions: RF power 150W, ICP power 150W, CHF3 30sccm, Ar 10sccm, H2 3sccm. The final measured etch rate was 25nm/min, etch duration 40minutes and final etch depth ~1000nm.

The final etched parallel waveguides had dimensions of 1µm wide , 850 µm long, 1 µm deep with a spacing between adjacent waveguides of 900nm. The overall device dimensions were 4mm wide , 4.850mm long and 503 µm thick (wafer thickness). The fluorine-based reactive ion etching recipe results in the formation and re-deposition of LiF which acts as an etch stop to the RIE process and inhibits further removal of material. In order to resolve this limitation on the process, a substrate reconditioning procedure based around a wet chemical cleaning solution made up of water, Hydrogen Peroxide and Ammonium Hydroxide was developed. By alternating the dry RIE and wet reconditioning processes, grooves of up to 3µm depth have been successfully fabricated.

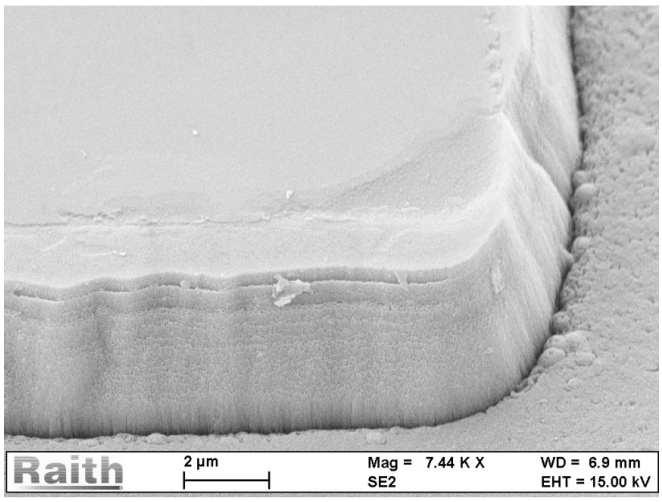

Fig. 7. Etched $LiNbO_3$ sample with alternating dry and wet etching in the presence of hydrogen to smooth the surface.

The introduction of hydrogen radicals into the plasma was found to reduce the overall roughness of the sidewalls as shown in Fig. 7. However, the addition of hydrogen causes a slight reduction in the overall etch rate due to the consumption of fluorine atoms to create HF molecules.

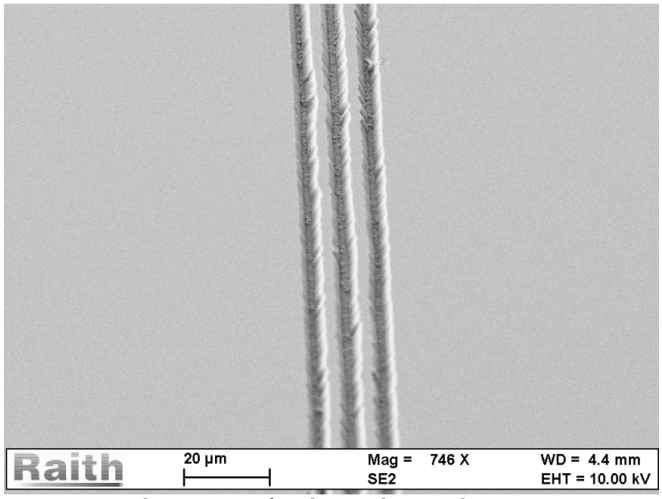

Fig. 8. Waveguide pattern transferred into Lithium Niobate using reactive ion etching.

The deposition of amorphous silicon was carried out in an Edwards 306 RF sputtering machine using a crystalline silicon target (99.9% purity). By manipulating the RF power of the sputtering process and thus the final density of the deposited a-Si, a degree of control of the final refractive index of the deposited amorphous silicon can be exercised. The RF sputtering of a-Si at different power levels leads to the formation of layers of increasing refractive index as a function of increasing power. A number of sample depositions were performed and the refractive indices of the thin (1µm) layers

were measured. RF powers of 200W and 250W produced refractive indices at 1550nm of 1.87 and 2.31 respectively. The modal analysis shown in Fig.1 and Fig. 2 used the 250W value of refractive index as it lay above the refractive index of the $LiNbO_3$.

After the deposition of a-Si, some back etching was required to remove the bridges of a-Si between the waveguide cores and the rest of the $LiNbO_3$ substrate surface. RIE etching was used to remove the bridge providing an even surface finish and removing material equally from all areas. The simulations of Fig. 1 and Fig. 2 show that the existence of a small subwavelength bridge will not significantly affect the waveguide performance so complete removal of the bridges was not required. Once the back etching was completed (Fig. 9), the waveguides were diced into 4mm x 4.85mm substrates using a fine grit dicing saw to give good optical quality to the input and output facets of the waveguide structure. Final assembly (Fig. 10) was completed using a customized glass carrier containing the input and output fibers capable of aligning the waveguides to the fiber cores with an accuracy of ±5µm.

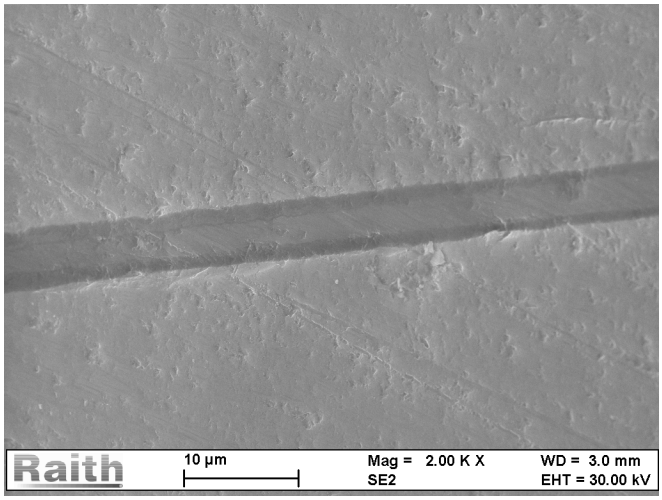

Fig.9. Waveguide after a-Si infill and back etching, the lighter part is the surface of the lithium niobate substrate.

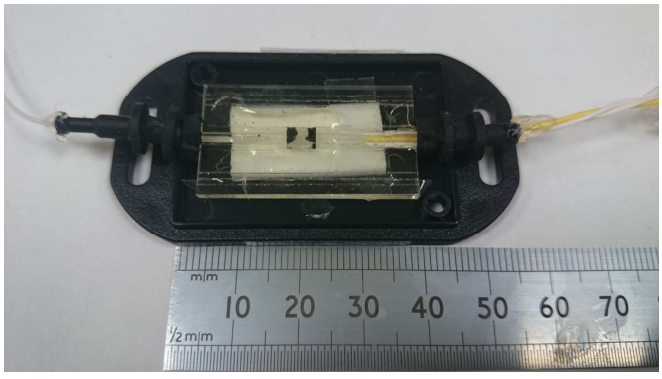

Fig.10.Assembly of complete sensor package.

III. RESULTS

The completed sensors were tested using an RF pulse generation system capable of producing pulses of up to 500kV/m with a double Gaussian profile of 50-200ns duration. By placing the sensors at different locations within a tapered region of the pulse generation system, different peak field strengths were achieved and the response of the sensor to these different fields could be assessed. The sensor worked as designed although some issues regarding the amplification of the detected optical signals are, at the time of writing, still being addressed – the overall loss of the optical system (from source laser to detector) is of the order of 60dB due primarily to a mode field mismatch between the single mode optical fiber and the a-Si/$LiNbO_3$ waveguides. The optical signal from the waveguides was detected using an off the shelf InGaAs high speed photodiode (ThorLabs DET08CFC) with a sub-ns (<70ps) rise time and a peak responsivity of 0.9A/W. A typical response of the sensor to an EMP is shown in Fig. 11 – in this case, the peak field strength was ~500kV/m although EMP detection was observed at each of the different peak field strengths investigated. The red trace is the triggering EMP; the blue trace is the detected optical signal from one of the waveguide output channels. The delay between the initial triggering pulse and the observed optical signal is 60ns corresponding to the path difference between the direct free-space path of the EMP trigger and the longer guided optical path of the sensor signal.

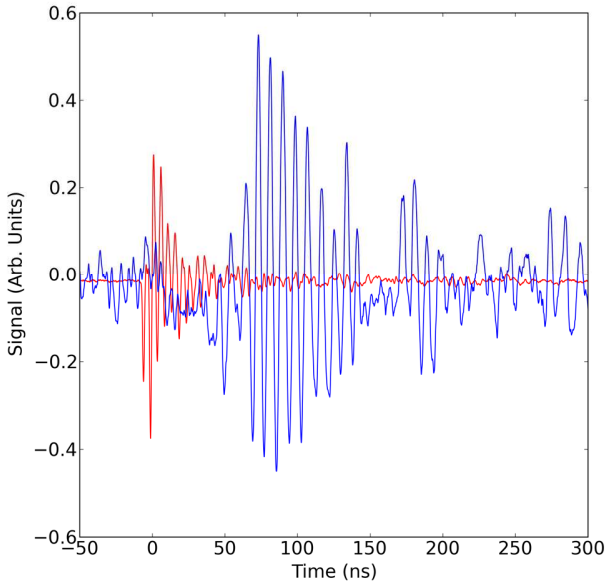

Fig.11.Temporal response from the sensor under 500kV/m EMP. The red trace is the triggering EMP pulse measured by a wire loop antenna and the blue trace is the output from one of the side channels of the waveguides.

The significant noise level in the measured signal has necessitated the development of a data processing algorithm that allows the removal of most of the noise without significantly impacting the waveform produced by the sensor. The algorithm used for noise removal is a thresholded short time Fourier transform (STFT) where a Fourier transform is applied to a moving temporal window across the duration of the signal. This method is similar in concept to the wavelet

transform [15] and produces a time-frequency spectrogram (Fig. 12) that shows the clear existence of the EMP induced variation separated from the background noise.

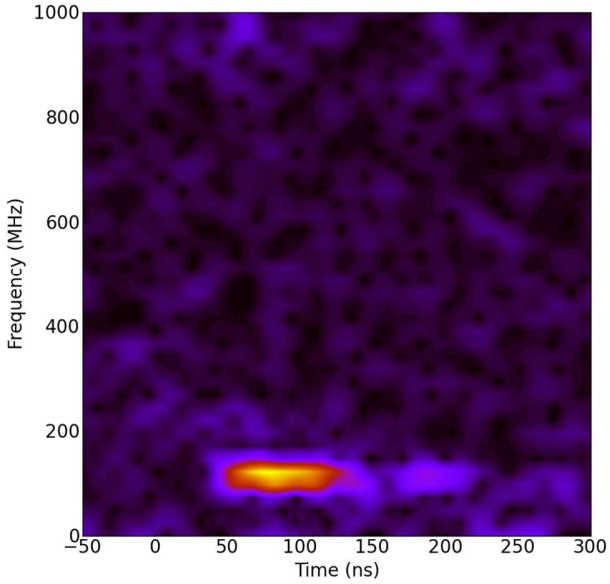

Fig. 12. Time-Frequency Spectrogram of the detected pulse (Fig. 11) measured by the waveguide sensor after noise removal by means of thresholded STFT.

The response of the sensor to peak EMP field strength was determined by plotting the peak measured voltage of two different coupling length sensors (450µm and 850µm respectively) as a function of the nominal EMP field strength (calculated by reference to the measured pulse strength). The results of this measurement can be seen in Fig. 13. The peak voltage is normalized by the detected optical power through the central sensor channel as the different sensors had different base levels of transmitted power. It can be seen that the trend of the measured sensor response appears to follow a generally sinusoidal pattern – this is primarily due to the existence of a low finesse cavity formed between the end facets of the waveguide structure and the optical fibers used to transfer the optical signal to and from the sensor. There are regions of the response curves where the monotonically increasing response would allow the determination of the peak EMP field strength over a limited range of field strengths. The replacement of the orthogonal waveguide facets with angled facets is a potential way to frustrate the low finesse cavity and improve the operating range of the sensor. In addition, the deployment of two sensors with different coupling lengths in parallel would allow the identification of the peak field strength over a much larger range of EMP field strengths.

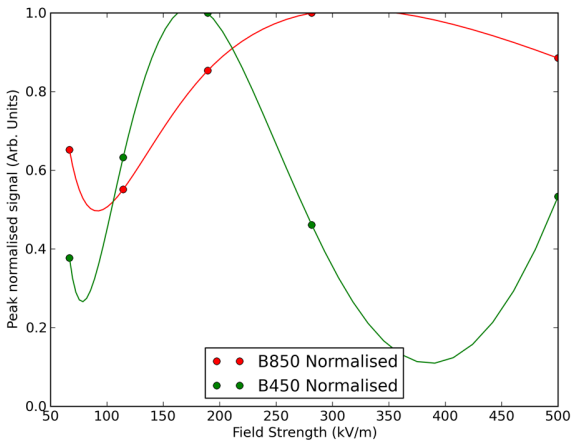

Fig. 13.Variation of peak measured sensor response as a function of peak EMP field strength.

IV. Conclusion

We have presented the design, fabrication and testing of an optical EMP sensor capable of determining both the temporal shape of the EMP as well as the peak field strength of the pulse. The use of $LiNbO_3$ as the substrate material has allowed the development of a compact sensor head compatible with powerful readily available laser sources and optoelectronic detection equipment. The fabrication processes needed to produce the desired waveguide structures have been characterized and fully optimized with a view to producing relatively large (~50) numbers of these sensors with standardized responses to the incident EMP. The processing of off-the-shelf $LiNbO_3$ substrates using standard photolithographic microfabrication techniques allows the creation of highly novel optically non-linear devices without the need for time consuming doping or expensive femtosecond machining. The integration of the sensor heads with the ancillary optical fiber equipment is still a relatively time consuming process as each assembly must be performed individually. From our experimental testing we have concluded that only a single output channel needs to be directly monitored and therefore only two fibers will need to be integrated with the sensor head in future rather than the current four. Further optimization of the fabrication and integration processes will reduce the overall size of the sensor head with a view to allowing the direct fusion splicing of the sensor head with the single input/output fiber channel.

References

[1] H.-M. Shen, R.W.P. King and T.T. Wu. “New Sensors for Measuring Very Short Electromagnetic Pulses.” *IEEE Trans on Antennas and Propagation.* 38(6), pp. 838-846, June 1990.

[2] E.L. Wooten, Karl M.Kissa, Alfredo Yi-Yan, Edmond J.Murphy. “A review of lithium niobate modulators for fiber-optic communications systems.” *IEEE J. of Selected Topics in Quantum Electronics.* 6(1), pp. 69-82, Feb. 2000.

[3] T.-C Lee, J.-T. Lee and M.A Roberta. “Surface acoustic wave applications of lithium niobate thin films.” *Appl. Phys. Letters.* 82(2), pp. 191-193, Jan. 2003.

[4] M. Luennemann, U. Hartwig, G. Panotopoulos and K.Buse. “Electrooptic properties of lithium niobate crystals for extremely high external electric fields.” Appl. Physics B. 76(4), pp.403-406, Apr. 2003.

[5] A. Lecestre, S. Benchabane, L.Robert, and R.Salut. “Electroplated Ni mask for plasma etching of sub micron features in lithium niobate.” *Microelectronic Engineering.* 105, pp. 95-98, May 2013.

[6] H .Hu, A.P Milenin, R.B. Wehrspohn, H. Hermann “Plasma etching of proton exchanged lithium niobate.” *J. Vac. Sci. Tech A.* 24(4), pp.1012-1015, Jun. 2006.

[7] G.J. Griffiths and R.J. Esdaile. “Analysis of Titanium diffused planar optical waveguides in Lithium Niobate.” *IEEE Journal of Quantum Electronics*. 20(2), pp. 149-159, Feb. 1984.

[8] R.V. Schmidt and I.P. Kaminov. “Metal diffused optical waveguides in $LiNbO_3$.” *Appl. Phys. Lett.*. 25(18), pp.458-460, Jun. 1974.

[9] M. L. Bortz and M.M. Fejer. “Annealed Proton-exchanged $LiNbO_3$ Waveguides.” *Opt. Lett.* 16(23) pp.1844-1846, Dec. 1991.

[10] R.R.Thomson, S. Campbell, I.J. Blewett, A.K. Kar and D.T. Reid.. “Optical waveguide fabrication in z-cut lithium niobate (LiNbO3) using femtosecond pulses in the low repetition rate regime.” *Appl. Phys. Lett.* 88(11), pp. 111109-111109-3, Mar. 2006.

[11] H. Lu, B. Sadani, N. Courjal, G. Ulliac. “Enhanced electro-optical Lithium Niobate photonic crystal wire waveguide on a smart cut thin film.” *Opt. Express.* 20(3), pp. 2974-2981, Jan. 2012.

[12] N. Courjal, F. Devaux, A. Gerthoffer, C.Guyot. “Low-loss $LiNbO_3$ tapered-ridge waveguides made by optical-grade dicing.” *Opt. Express.* 23(11), pp. 13983-13990, Mar. 2015.

[13] W-P Huang. “Coupled Mode Theory For Optical Waveguides: an Overview.” *J.Opt.Soc.Am.A* 11(3), pp. 963-983, Mar. 1994.

[14] S. Somekh, E. Garmire, A. Yariv, H.L. Garvin, and R.G. Hunsperger. “Channel Optical Waveguides and Directional Couplers in GaAs-lmbedded and Ridged”. *Appl. Opt.* 13(2), pp.327-330, Feb. 1974.

[15] S. Qian, “Introduction to Time-Frequency and Wavelet Transforms”, 1st ed., Prentice Hall, 2002.

[16] M. Lohmeyer.. “Wave-matching-method for mode analysis of dielectric waveguides.” *Opt. and Quant. Elec.* 29(9), pp. 907-922, Sep.1997.

BIOGRAPHIES

Andrew J. Waddie received his B.Sc. in Natural Philosophy and Physics from the University of Edinburgh in 1990, M.Sc. in Computing and Computer Modeling of Optoelectronic Materials and Devices from the University of Newcastle-upon-Tyne in 1991 and his Ph.D. in Optoelectronic Neural Networks from Heriot-Watt University in 1996.

Since 1996 he has been employed as a Research Associate in the Diffractive Optics group of the Institute of Photonics and Quantum Sciences (IPaQS), School of Engineering and Physical Sciences, Heriot-Watt University. His research interests include diffractive and micro-optical design and fabrication, optoelectronic systems, optical beam shaping and computational electromagnetism. He has published over 80 papers in scientific journals and conference proceedings (both contributed and invited). He is a member of the Optical Society of America, the Society of Photonic and Instrumentation Engineers and the UK Institute of Physics.

Adrian Dzipalski is a Ph.D. student in the Diffractive and Micro-Optics Group of the Institute of Photonics and Quantum Sciences (IPaQS), School of Engineering and Physical Sciences, Heriot-Watt University. His research interests include fiber optic sensors, micro- and nano-fabrication and micro-optics.

Iain Thurston : biography not available at this time.

Michael Moutrie : biography not available at this time.

Mohammad R. Taghizadeh received his Ph.D. from Heriot-Watt University in 1982. Since 1985 he has been a member of faculty at the Institute of Photonics and Quantum Sciences (IPaQS), School of Engineering and Physical Sciences, Heriot-Watt University where he is currently the head of Diffractive and Micro-Optics Group. His research interests include the design, fabrication and application of diffractive and refractive optical elements, optical information processing and optical interconnects. Prof. Taghizadeh has published over 300 papers in scientific journals and presented many invited papers at international conferences. He has also acted as a conference chair and technical committee member of numerous international conferences.